Deep Resources Engineering 2 (2025) 100206

Contents lists available at ScienceDirect

Deep Resources Engineering

journal homepage: www.keaipublishing.com/en/journals/deepre/

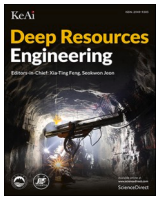

Dynamic fracture behavior of rock tunnel under impact loading: Insights from experiments and peridynamic simulations

Peng Ying [a,e], Yu Zhao [b], Junchen Zhang [b], Weijian Li [b,*], Yiqiang Zhao [d], Zheming Zhu [c], Yanliang Du [b]

[a] State Key Laboratory of Intelligent Geotechnics and Tunnelling, Southwest Jiaotong University, Chengdu 610031, China
[b] National Key Laboratory of Green and Long-Life Road Engineering in Extreme Environment, Shenzhen University, Shenzhen 518060, China
[c] State Key Laboratory of Hydraulics and Mountain River Engineering, School of Architecture and Environment, Sichuan University, Chengdu 610065, China
[d] Guiyuan Environmental Technology Co. Ltd., Jinhua 322300, China
[e] Zhejiang Jiaotou Expressway Construction Management Co., LTD, Hangzhou, China

ARTICLE INFO

Keywords:
Rock tunnel
Crack propagation
Rock dynamics
Peridynamic model
Stress wave

ABSTRACT

The dynamic response of fractured rock masses with tunnel-like holes under impact loading is critical for ensuring the stability of underground engineering structures. This study investigates the interplay between stress waves, crack propagation, and hole defects in rock materials through a combined experimental and numerical approach. A novel Large Single Cleavage Semicircle Compression (LSCSC) test is designed using U-shaped holed specimens with prefabricated cracks, enabling precise measurement of crack propagation velocity via crack propagation gauges (CPGs). An extended peridynamic (XPD) model with a local strain based implementation is introduced to simulate dynamic fracture processes under varying tunnel orientations. The results demonstrate that hole defects significantly alter crack patterns and reduce fracture toughness, with an inverse correlation between crack propagation speed and fracture toughness. Notably, the specimen exhibits the highest susceptibility to failure when the tunnel is inclined at a 45° angle to the stress wave direction. The experimental and numerical results align closely, validating the XPD model's capability to capture stress heterogeneity, crack initiation, and dynamic failure modes. This work provides critical insights into the fracture mechanisms of holed rock structures under dynamic loads, offering practical references for hazard mitigation in tunneling and underground engineering.

1. Introduction

The mechanical behavior of rock is a topic of fundamental importance with numerous engineering applications, such as tunneling, mining, and other underground projects. Rock materials are heterogeneous, comprising various geological structures, such as joints, faults, and micro-cracks [1,2]. Both natural defects and man-made defects caused by engineering activities are the focus of rock mechanics. The size, arrangement, and formation of these defects can significantly affect the stability of rock structures. It is noted that under dynamic loading, cracks may initiate and propagate more rapidly compared to static conditions. Moreover, the existence of holes/tunnels near the crack propagation path can alter the fracture behavior, making the failure mechanism more complex [3,4]. Therefore, it is crucial to investigate the influence of these defects on rock failure behavior under dynamic loading conditions.

The dynamic response under impact loading is a complex process involving multidisciplinary research, including rock dynamics, damage mechanics, and stress wave theory [5]. Xu and Li conducted compression tests on rock samples with elliptical defects, revealing that different shapes of defects lead to varying failure modes and crack propagation paths [6]. To explore the influence of different pore shapes, Zhang et al. used the two-dimensional particle flow code (PFC) to study the failure characteristics of samples. The results indicate that stress concentration zones appear around hole defects during loading, leading to crack initiation and specimen failure [7]. Wasantha et al. [8] built samples with pre-cracks and holes under uniaxial compression using the Universal Distinct Element Code (UDEC) software to study the effect of pre-cracks or holes on mechanical response. The results show that the presence of holes plays a major role in crack initiation. Jia and Tang [9] studied the failure mechanism of rock masses, revealing that defects significantly influence the failure mode of tunnels by analyzing the rock

* Corresponding author.
E-mail address: weijianli@szu.edu.cn (W. Li).

https://doi.org/10.1016/j.deepre.2025.100206
Received 17 February 2025; Received in revised form 22 June 2025; Accepted 21 July 2025
Available online 5 August 2025

failure process. These studies provide important guidance for engineering designs, especially for underground spaces where experiments are difficult to conduct. However, they mainly focus on the mechanical behavior of rocks under static or quasi-static loading. In reality, rocks are often subjected to dynamic loading, which can lead to more complex failure behavior [10,11]. Zhou et al. [12] found that more diverse failure modes may occur in cracked tunnels under dynamic loading compared to static conditions. Li et al. [13] discovered that when a hole is subjected to plane waves, the crack expands parallel to the direction of the incident wave. Ying et al. [14,15] used a drop weight test system to study the fracture behavior of rocks, finding that the fracture behavior is related to environmental factors and loading rate.

When full-scale experiments are either prohibitively expensive or not feasible, computational modeling emerges as an essential tool for predicting the deformation of solids and gaining insights into the deformation mechanism. Nevertheless, the numerical analysis methods described in existing literature mainly rely on traditional techniques. For instance, the finite element method (FEM) can be used to analyze complex structural mechanics problems. However, it often encounters difficulties in simulating large deformations and material failure processes. The finite difference method (FDM), which is flexible in dealing with fluid flow or soil landslide problems, encounters limitations in rock engineering for its inconvenience of applying boundary conditions and the high requirement for grid density. The discrete element method (DEM) can simulate the propagation trends of cracks, yet it still struggles with unresolved mechanical issues, making it challenging to precisely predict the behavior of solid materials. This paper applies the peridynamic(PD) method to model the dynamic solution of specimens with man-made tunnel-like holes. Both fracture behavior and material response are studied for comparison with experimental results. The peridynamic method, one of the most promising numerical methods, has been studied by many researchers for its outstanding performance in predicting fracture behavior while maintaining consistency with continuum mechanics [16,17]. In PD theory, the differential equation in traditional continuum methods is replaced by the bond force integral equation of PD, avoiding singularity when facing discontinuities. The nonlocal feature of peridynamics makes it an effective method in dealing with various boundary value problems [18–21]. However, in the classical version of the peridynamic model, two nodes are connected by a one-dimensional bond, resulting in a fixed Poisson's ratio. The extended peridynamic (XPD) method proposed in [22,23] addresses this constraint by enriching the original model with a shear strain term. A local strain-based implementation is proposed to remove the rigid rotation part in bond relative displacements. Validation of its predictive ability in brittle fracture problems can be found in [23–25].

In this study, the mechanical behavior of holed specimens under dynamic compressive loading is investigated. The test is designed to study the influence of different holes in the crack propagation path on material fracture behavior. A hybrid drop weight test system based on the design principle of SHPB was applied for the impact test. Crack propagation gauges (CPGs) were attached to the proposed crack propagation location to record specific response data. The extended peridynamic method is applied to simulate crack initiation and extension behavior. The crack initiation characteristics, crack patterns, and propagation behavior for various types of specimens were analyzed, and the validity was confirmed by comparing the numerical results with the test results.

2. A drop weight test system

To investigate the dynamic fracture behavior of holed rock specimens under impact loading, notched specimens with and without holes were introduced, and a drop-weight system was implemented.

The experimental system primarily consists of two main components. The first is the drop impact system, which includes an impact plate, wave shaper, incident plate, transmission plate, and amortisseur, as illustrated in Fig. 1a. The second component is the acquisition system, comprising a processor, oscilloscope, voltage regulator source, and ultra-dynamic strain gauge, as shown in Fig. 1b. Both the incident and transmission plates are made of LY12CZ aluminum alloy. An electronic infrared speedometer is utilized to measure the impact velocity of the drop hammer. In the physical test, the specimen is positioned between the incident and transmission plates. Strain gauges SG_i and SG_t are attached to the centers of the incident plate and transmission plate, respectively, and connected to the data acquisition system. The working principle of the strain gauges is as follows: when the drop weight impacts the incident plate, the strain gauge on the incident plate deforms. This deformation is amplified by an ultra-dynamic strain amplifier and then transmitted to the oscilloscope. The voltage signal is subsequently derived from the oscilloscope to the workstation, allowing the deformation of the strain gauge to be determined

$$\varepsilon = \frac{4U_0}{nE_gK} \tag{1}$$

where ε is the strain gauge test variable, U_0 is the measured voltage from the strain gauge, $E_g = 2\text{V}$ is the bridge supply voltage, $K = 2$ is the strain gauge sensitivity coefficient, and $n = 1000$ is the gain coefficient of the amplifier.

According to the stress wave theory and the principle of the split Hopkinson pressure bar, the stress data acting on the upper ends of the specimen can be obtained as follows:

$$\sigma_{\text{I}} = A_{\text{i}}E_P(\varepsilon_i(t) + \varepsilon_r(t)) \tag{2}$$

where E_P is the elasticity modulus of the aluminum alloy plate, $\varepsilon_i(t)$and $\varepsilon_r(t)$ are the strains recorded from the strain gauges attached to the center of the incident plate, and A_i is the contact area between the specimen and the incident plate. The experimental results of the incident loading waves in the specimen are presented in Fig. 2.

To measure the crack extension speed, a crack propagation gauge (CPG) was used. In this study, two types of CPGs, BKX5–10CY-21 (for specimens without holes) and BKX3–10CY-10 (for specimens with holes), were employed. These CPGs are connected with 21 grid wires (BKX5–10CY-21) and 11 grid wires (BKX3–10CY-10) in parallel, as shown in Fig. 3. The parameters of the CPGs are displayed in Table 1. The CPGs were arranged in the direction of the crack propagation path, with the first wire overlapping the pre-crack tip. As the crack initiates and propagates, it breaks the grid wires sequentially, creating a series of signal steps in the acquisition system. The crack extension speed is then measured by the ratio of the distance between two adjacent grid wires to the time.

3. The extended peridynamic method (XPD)

In the peridynamic framework, a solid occupying the domain Ω is discretized by a finite number of particles. Two related particles are connected to each other via a bond. When the local equilibrium condition is concerned, an integral term in terms of the force density function $\boldsymbol{f}(\boldsymbol{x},t)$is introduced to replace the stress-related partial differential term in continuum solid mechanics. In virtue of the Newton's second law, the motion equation of material particle $\boldsymbol{x}$ at instant t is written in the form:

$$\rho\ddot{\boldsymbol{u}}(\boldsymbol{x},t) = \int_{\mathcal{H}_x} \boldsymbol{f}(\boldsymbol{x},t)\mathrm{d}V_{x'} + \boldsymbol{b}(\boldsymbol{x},t), \quad \boldsymbol{x} \in \Omega \tag{3}$$

where ρ is the mass density, $\ddot{\boldsymbol{u}}$ is the acceleration vector, and $\boldsymbol{b}$ is the body force density. $\mathcal{H}_x$ is the horizon of radius δ associated with the material point $\boldsymbol{x}$, as shown in Fig. 4.

The integral term $\int_{\mathcal{H}_x}\boldsymbol{f}(\boldsymbol{x},t)\mathrm{d}V_{x'}$ can thus be measured by means of the forces transmitted through the bonds that connect the particle $\boldsymbol{x}$.

Let us consider two particles in the same horizon and initially with the respective locations $\boldsymbol{x}$ and $\boldsymbol{x}'$, which define the relative position vector

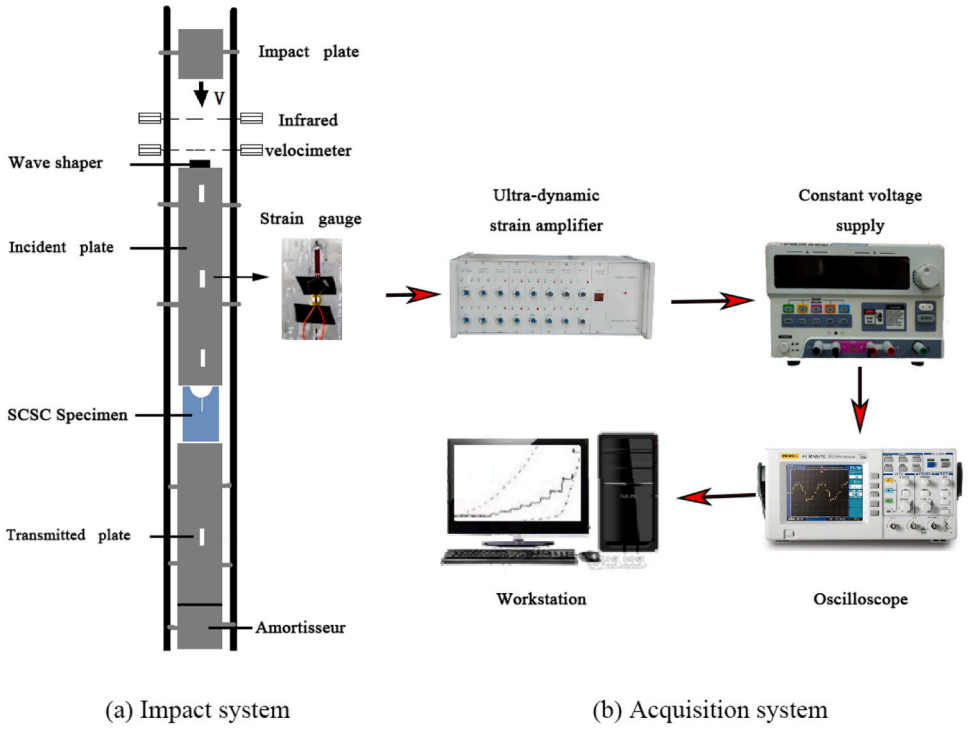

Fig. 1. The experimental system.

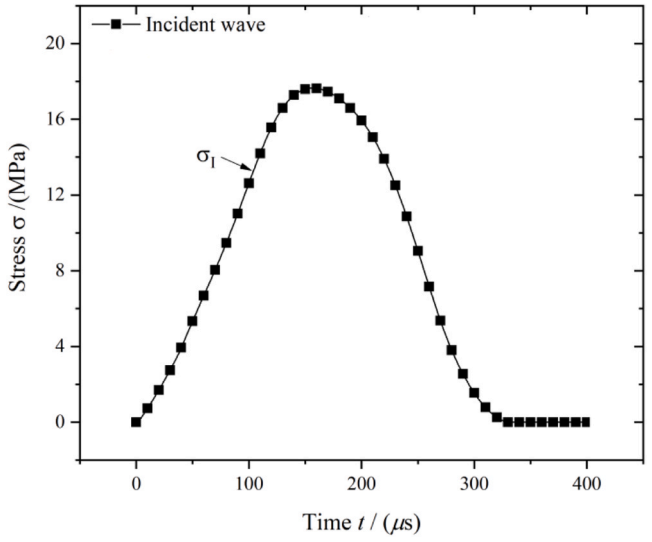

Fig. 2. Incident and transmission loading waves in the specimen.

$$\boldsymbol{\xi} = \boldsymbol{x}' - \boldsymbol{x} \tag{4}$$

Assume that at instant t , these two particles have displaced with $\boldsymbol{u}(\boldsymbol{x}, t)$ and $\boldsymbol{u}(\boldsymbol{x}', t)$, respectively. It is now possible to define the relative displacement vector

$$\boldsymbol{\eta} = \boldsymbol{u}(\boldsymbol{x}', t) - \boldsymbol{u}(\boldsymbol{x}, t) \tag{5}$$

which is actually related to some local deformation of solid.

In the linearly elastic regime, the local force density function can be formulated as

$$\boldsymbol{f}(\boldsymbol{\eta}, \boldsymbol{\xi}, t) = \mathbf{C} \cdot \boldsymbol{\eta} \tag{6}$$

where $\mathbf{C}$ denotes the second order bond stiffness tensor.

In [22,23], an extended peridynamic model (XPD) is proposed to tackle the limitation of Poisson's ratio by involving local shear

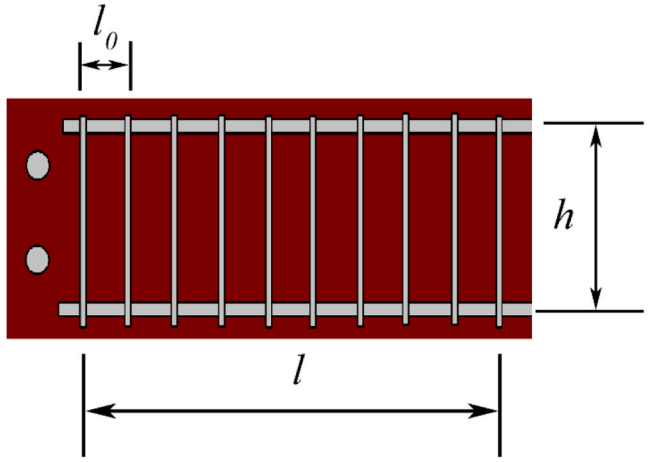

Fig. 3. The schematic of CPG.

Table 1
The two types of CPG parameters.

CPG type	Specimen	l (mm)	h (mm)	l_0 (mm)
BKX5–10CY–21	No hole	40	10	2
BKX3–10CY–10	With hole	10	10	1

deformation via bond rotation, the tensor becomes

$$\mathbf{C} = \frac{1}{\xi}[c\boldsymbol{n} \otimes \boldsymbol{n} + \kappa(\boldsymbol{I} - \boldsymbol{n} \otimes \boldsymbol{n})] \tag{7}$$

where $\xi = \|\boldsymbol{\xi}\|$, and $\boldsymbol{n} = \boldsymbol{\xi}/\xi$ is the normal vector in bond direction. Further, $\otimes$ denotes the tensor product operation and the components of $\boldsymbol{n} \otimes \boldsymbol{n}$ are $n_i n_j$, $i, j = 1, 2, 3$. In Eq. (7), $\boldsymbol{I}$ denotes the second order identity tensor, that is $I_{ij} = 1$ when $i = j$, and $I_{ij} = 0$, otherwise.

In addition, c and κrepresent the bond stiffness moduli in the stretch and shear directions, respectively. And in isotropic context they can be

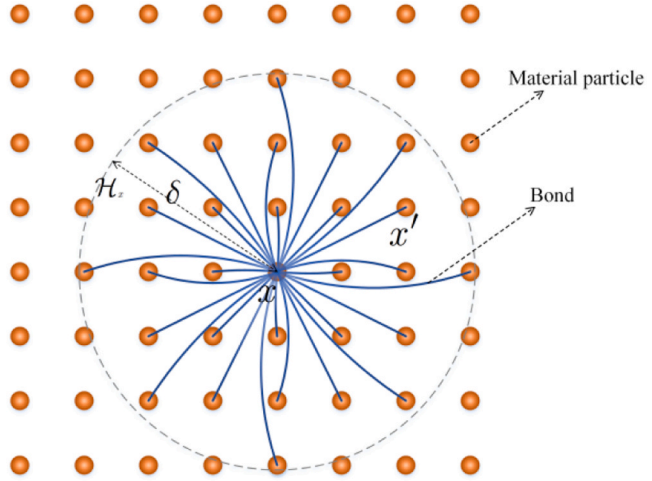

Fig. 4. Distribution of PD particles and definition of the horizon.

determined in terms of the elastic constants like the Young's modulus $E$and Poisson's ratio ν of solid body. For plane stress problems:

$$c = \frac{6E}{\pi\delta^3(1-\nu)}, \kappa = \frac{6E(1-3\nu)}{\pi\delta^3(1-\nu^2)} \tag{8}$$

and for plane strain problems:

$$c = \frac{6E}{\pi\delta^3(1+\nu)(1-2\nu)}, \kappa = \frac{6E(1-4\nu)}{\pi\delta^3(1+\nu)(1-2\nu)} \tag{9}$$

3.1. Description of local deformation

From geometric viewpoints, the relative displacement vector $\boldsymbol{\eta}$ can be divided into a normal part and a tangential part, such that

$$\ell = \frac{1}{\xi}\boldsymbol{\eta}\cdot\boldsymbol{n} \tag{10}$$

and

$$\boldsymbol{\gamma} = \frac{1}{\xi}(\boldsymbol{\eta} - (\boldsymbol{\eta}\cdot\boldsymbol{n})\boldsymbol{n}) \tag{11}$$

On the other hand, $\boldsymbol{\eta}$ can be related linearly to the local strain tensor $\boldsymbol{\varepsilon}$

$$\boldsymbol{\eta} = \boldsymbol{\varepsilon}\cdot\boldsymbol{\xi} \tag{12}$$

In this sense, the relative displacement $\boldsymbol{n}$ can be physically interpreted as local deformation vector. Accordingly, the normal and tangential components l and y are also formulated in terms of the local strain

$$\ell = \boldsymbol{n}\cdot\boldsymbol{\varepsilon}\cdot\boldsymbol{n}$$

$$\boldsymbol{\gamma} = \boldsymbol{n}\cdot\boldsymbol{\varepsilon}\cdot(\boldsymbol{I} - \boldsymbol{n}\otimes\boldsymbol{n}) \tag{13}$$

3.2. Bond failure criterion

For describing bond failure, a characteristic function $\mu(\boldsymbol{u},\boldsymbol{\xi})$ is introduced into the force-relative displacement relation $\boldsymbol{f}(\boldsymbol{u},\boldsymbol{\xi}) = \mu(\boldsymbol{u},\boldsymbol{\xi})[c\ell\boldsymbol{n} + \kappa\boldsymbol{n}\cdot\boldsymbol{\varepsilon}\cdot(\boldsymbol{I}-\boldsymbol{n}\otimes\boldsymbol{n})]$ with

$$\mu(\boldsymbol{u},\boldsymbol{\xi}) = \begin{cases} 1, & \text{if} \ell < \ell_c \text{ and } \|\boldsymbol{\gamma}\| < \gamma_c \\ 0, & \text{if} \ell \geq \ell_c \text{ or } \|\boldsymbol{\gamma}\| > \gamma_c \end{cases} \tag{14}$$

where ℓ_c and γ_c are the critical values of the bond stretch and bond rotation, respectively.

According to [17], the local damage variable $d(\boldsymbol{x})$ at particle $\boldsymbol{x}$ is defined in the form

$$d(\boldsymbol{x}) = 1 - \frac{\int_{\mathcal{H}_x}\mu(\boldsymbol{u},\boldsymbol{\xi})\mathrm{d}V_{x'}}{\int_{\mathcal{H}_x}\mathrm{d}V_{x'}} \tag{15}$$

3.3. Solution of dynamic problems

The numerical solution of dynamic problems can be obtained using the central difference time-integration method, or the Verlet-velocity algorithm [26]:

$$\begin{aligned} \dot{\mathbf{U}}^{n+\frac{1}{2}} &= \dot{\mathbf{U}}^{n-\frac{1}{2}} + \Delta t\ddot{\mathbf{U}}^n \\ \mathbf{U}^{n+1} &= \mathbf{U}^n + \Delta t\dot{\mathbf{U}}^{n+\frac{1}{2}} \end{aligned} \tag{16}$$

where $\dot{\mathbf{U}}$ is the velocity column matrix and $\ddot{\mathbf{U}}$ is the acceleration column matrix. To ensure numerical stability, the time step Δt is constrained by

$$\begin{aligned} \Delta t &\leq \frac{\Delta_{min}}{c_k} \\ c_k &= \sqrt{K/\rho} \end{aligned} \tag{17}$$

where Δ_{min} is the minimum node distance in the discrete domain and K is the bulk modulus. Combining the force-displacement relationship of the system

$$\begin{aligned} \mathbf{F} &= \mathbf{K}\mathbf{U} \\ \ddot{\mathbf{U}} &= \frac{\mathbf{F}}{m} \end{aligned} \tag{18}$$

m represents the mass of each particle in the uniform grid.

Alternatively, the explicit iterative format of the Newmark method [27] can also be used:

$$\begin{aligned} \dot{\mathbf{U}}^n &= \dot{\mathbf{U}}^{n-1} + \Delta t\left(\frac{1}{2}\ddot{\mathbf{U}}^{n-1} + \frac{1}{2}\ddot{\mathbf{U}}^n\right) \\ \mathbf{U}^{n+1} &= \mathbf{U}^n + \Delta t\dot{\mathbf{U}}^n + \frac{(\Delta t)^2}{2}\ddot{\mathbf{U}}^n \end{aligned} \tag{19}$$

In the examples of this paper, there is no significant difference between the results calculated by the above two formats. In addition, the deformation of each extended bond can be obtained from the displacements of related material points. Subsequently, new broken bonds can be obtained according to the fracture criterion, and then the relevant particle list of each point and the corresponding local stiffness are

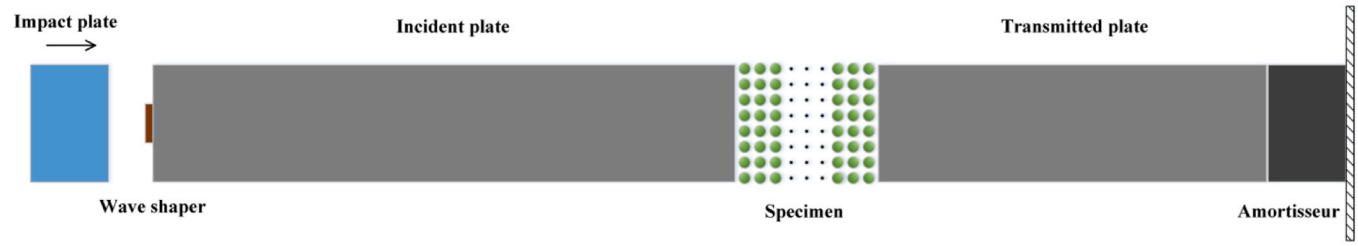

Fig. 5. Impact system.

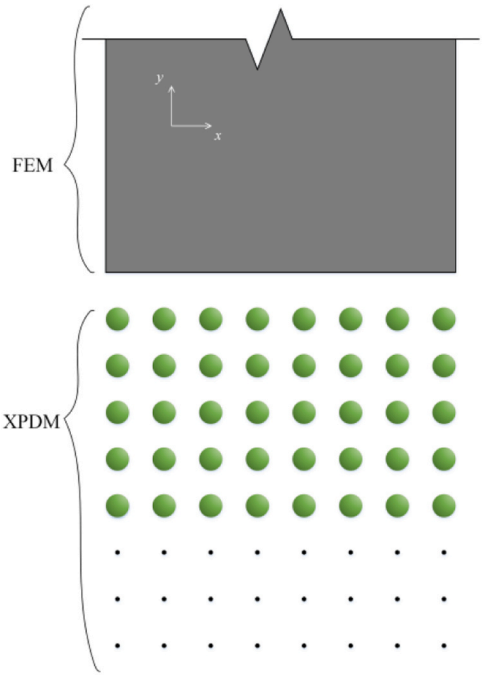

Fig. 6. Diagram of the collision model.

updated.

4. Numerical model of the impact test

4.1. Introduction to the impact system

The numerical model of drop weight impact system is composed of an impact plate (drop hammer), a wave shaper, an incident plate, a transmission plate, and a damper, as shown in Fig. 5.

The specimen consists of simulated structures made of various types of rocks, which interact with the incident plate and transmission plate through contact.

In the Data Acquisition System, collection points are set on the incident plate to detect the waveform of the incident wave and the

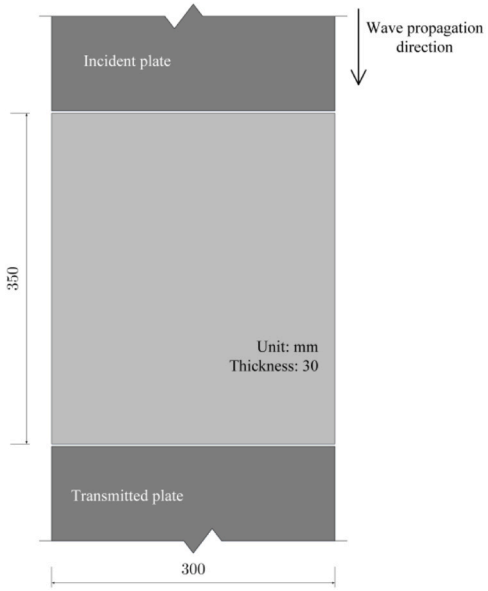

Fig. 7. The geometry of a non-porous plate.

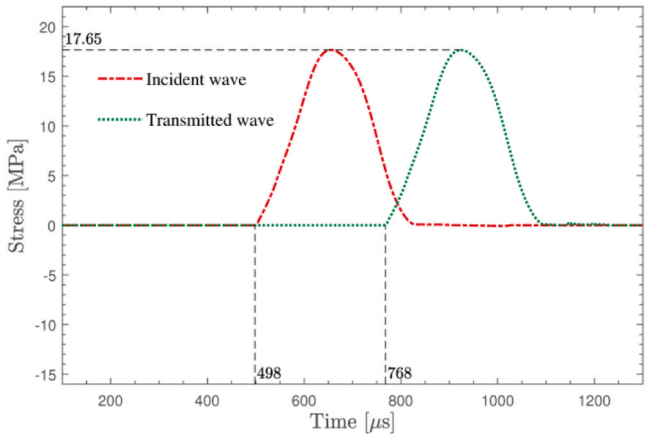

Fig. 8. Incident wave and transmitted wave ($E = 71.7$GPa, $\nu = 0.17$and $\rho = 2850$kg/m^3).

influence of the reflected wave. Additionally, a recording point is set on the transmission plate to record the waveform of the transmitted wave. Leveraging the advantages of numerical simulation, the distribution changes of contact forces between the plates and the specimen are also recorded.

The drop hammer impacts downward from the top, generating a relatively smooth sine wave through the shaper. The incident and transmission plates are made of aluminum alloy with an elastic modulus of 71.7 GPa and a density of 2850 kg/m^3 , so the propagation speed of the stress wave in the plates is

$$v_L = \sqrt{\frac{E}{\rho}} = \sqrt{\frac{71.7 \times 10^9}{2850}} \approx 5015 \text{ m} \Big/ \text{s} \tag{20}$$

The dimensions of the incident plate are $3m \times 0.3m \times 0.03m$, and the time required for the stress wave to propagate from the top of the incident plate to the specimen is 598 us. The dimensions of the transmission plate are $2m \times 0.3m \times 0.03m$, and the time required for the stress wave to propagate from the specimen to the damper is 399 us. Since the lengths of the incident and transmission plates are much greater than their widths, they can be approximated as one-dimensional finite element models. The stress field and damage field of the specimen under dynamic impact constitute the primary focus of our numerical analysis, which is conducted using the peridynamic method. It is important to note that in the simulation of this dynamic system, the incident plate, transmission plate and specimen must adopt the same grid spacing. The stiffness of the incident and transmission plate elements is given by:

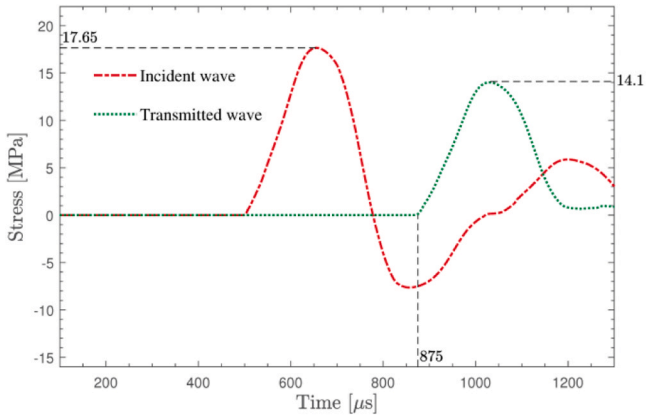

Fig. 9. Incident wave and transmitted wave ($E = 11.1$GPa, $\nu = 0.17$ and $\rho = 2850$kg/m^3).

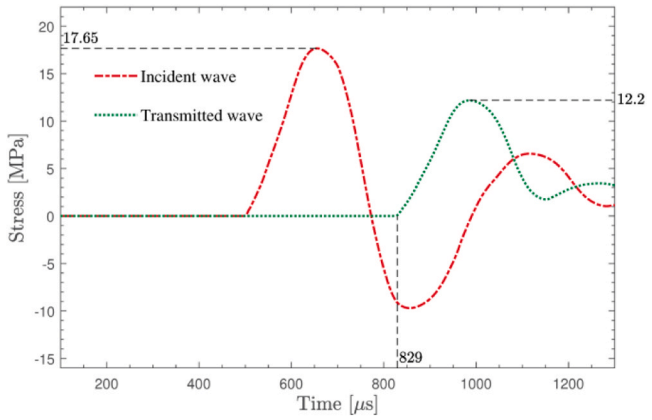

Fig. 10. Incident wave and transmitted wave ($E = 11.1$GPa, $\nu = 0.17$ and $\rho = 1550$kg/m^3).

$$K_1 = E_r \times A_r/\Delta x \tag{21}$$

where E_r is the elastic modulus of the incident plate , A_r is the cross-sectional area of the plate, and Δx is the element size.

4.2. Collision model

The schematic diagram of collision surface between the plate and the sample is shown in Fig. 6. Assuming the y-direction displacement of the lower end face of the incident plate is u_r, and the displacement of the material point in the y-direction on the upper end face of the specimen is u_i, then the force applied to the specimen is

$$f_i = 0.5 \times c_c[(u_r - u_i) - ||u_r - u_i||], i = 1, 2, \ldots, n \tag{22}$$

Then the reaction force at the bottom end of the incident rod is

$$f_r = -\sum_{i=1}^{n} f_i \tag{23}$$

Assuming the y-direction displacement of the upper end face of the transmission plate is u_t, and the displacement of the material point in the y-direction on the lower end face of the specimen is u_j, then the force

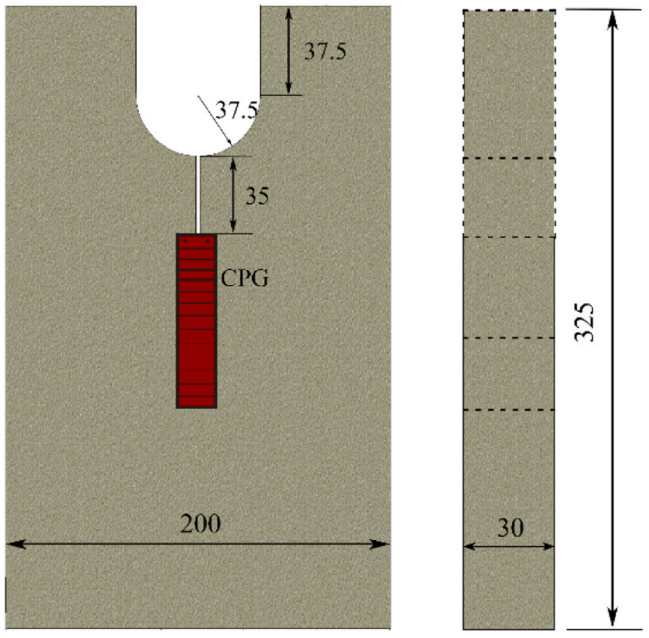

Fig. 11. Geometric sketch of the sample (unit: mm).

Table 2
Parameters used in the numerical simulations.

$E_{(\mathrm{GPa})}$	ν	$\rho^3_{(\mathrm{kg/m})}$	ℓ_c	$\delta_{(\mathrm{mm})}$	Δx (mm)
13.5	0.22	2347	0.0021	3	1

applied to the lower end of the specimen is

$$f_j = -0.5 \times c_c[(u_j - u_t) - ||u_j - u_t||], j = 1, 2, \ldots, n \tag{24}$$

Then, the reaction force received at the top end of the transmission rod is

$$f_r = -\sum_{j=1}^{n} f_j \tag{25}$$

The contact stiffness is taken as $c_c = EA/\Delta x$, where E is the elastic modulus of the sample , $A = h\Delta x$ is the cross-sectional area of the unit material point, and h is the thickness of the sample.

4.3. Validation of the numerical system

To verify the effectiveness of this model, we employed a complete plate sample placed between the incident and transmission plates to test the transmission of stress waves in the impact system, as illustrated in Fig. 7. The dimensions of the plate are 350 mm in height, 300 mm in width, and 30 mm in thickness, with the material properties identical to those of the incident and transmission plates.

A stress wave was applied from the top of the incident plate, and Fig. 8 records the stress changes caused by the stress wave at the recording points on the incident and transmission plates. The recording point on the incident plate is located 2.5 m from the top of the incident plate, with a simulated arrival time of the incident wave is 498 us, which matches the theoretical result:

$$t = \frac{2.5}{5015} \approx 498 \times 10^{-6} s \tag{26}$$

The recording point on the transmission plate is located 0.5 m from the top of the transmission plate, with the simulated arrival time of the incident wave consistent with the theoretical value:

$$t = \frac{3 + 0.35 + 0.5}{5015} \approx 768 \times 10^{-6} s \tag{27}$$

Here we will also compare the differences between the wave in the transmission plate and that in the incident plate from both theoretical and numerical perspectives.

The impedance of a plate is:

$$Z = \rho v_L \tag{28}$$

When a wave propagates from the incident plate to the specimen, the transmission coefficient is:

$$T_1 = \frac{2Z_{\mathrm{spec}}}{Z_{\mathrm{in}} + Z_{\mathrm{spec}}} \tag{29}$$

When a wave propagates from the specimen to the transmitted plate, the transmission coefficient is:

$$T_2 = \frac{2Z_{\mathrm{tran}}}{Z_{\mathrm{spec}} + Z_{\mathrm{tran}}} \tag{30}$$

When the wave undergoes transmission twice through the incident plate-specimen interface and the specimen-transmission plate interface, the total transmission coefficient is

$$T_t = T_1 \times T_2 \tag{31}$$

Therefore, in the case that material property of the specimen is identical to those of the incident and transmission plates, the total transmission coefficient is 1. Fig. 8 shows that the simulated incident

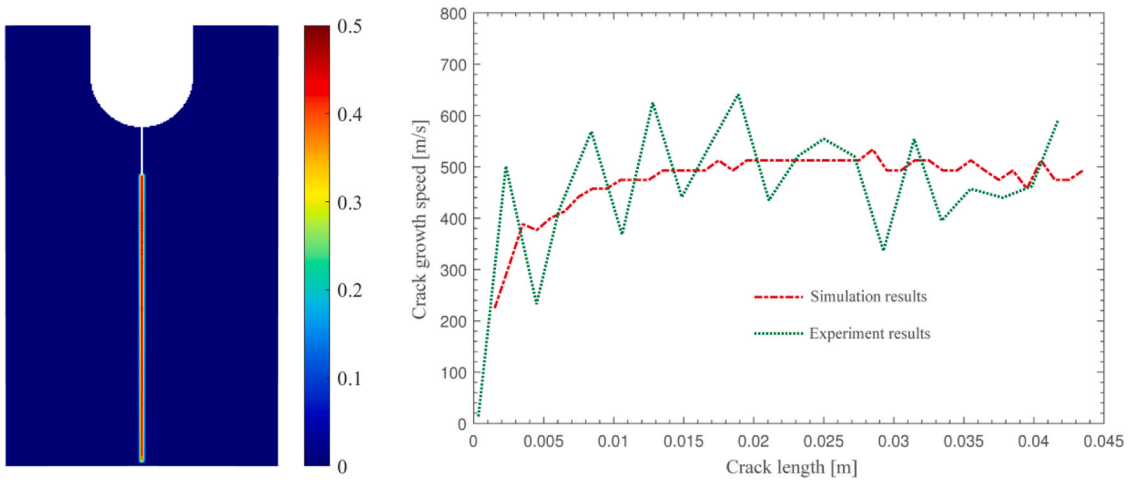

Fig. 12. The crack propagation response of samples without holes.

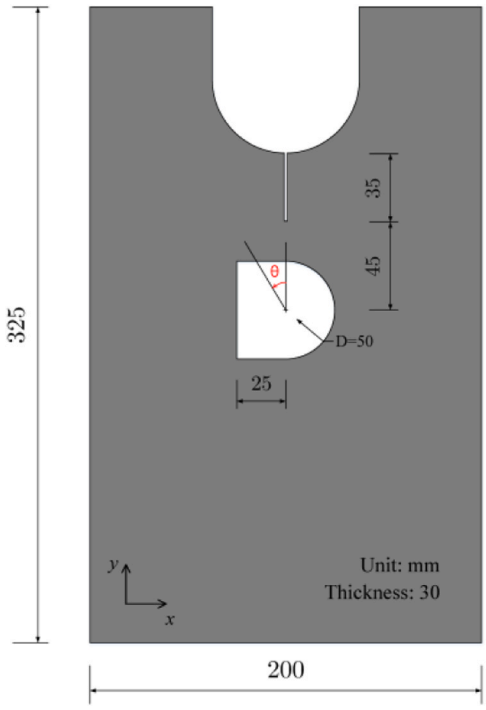

Fig. 13. The sample with a prefabricated crack outside the tunnel.

wave is identical to the transmitted wave, which is consistent with the theoretical result.

Upon changing the sample material, for a material with an elastic modulus of 11.1GPa, a Poisson's ratio of 0.17, and a density of $2850kg/m^3$, the wave speed is $\sqrt{11.1\times10^9/2850}\approx1974$ m/s, and the time at which the incident wave reaches the recording point on the transmission plate is

$$t=\frac{3+0.5}{5015}+\frac{0.35}{1974}\approx875\times10^{-6}s \tag{32}$$

In this case, through Equations (28)—(31), the theoretical total transmission coefficient is derived as $T_t = 0.81$.

As shown in Fig. 9, the ratio of the amplitude of the simulated transmitted wave to that of the incident wave is $14.1/17.65\approx0.8$. Both the arrival time of the wave and the amplitude attenuation ratio of the transmitted wave match well with the theoretical solutions.

For a sample with an elastic modulus of 11.1GPa, a Poisson's ratio of 0.17 and a density of $1550kg/m^3$, the time at which the incident wave reaches the recording point on the transmission plate is

$$t=\frac{3+0.5}{5015}+\frac{0.35}{\sqrt{11.1\times10^9/1550}}\approx829\times10^{-6}s \tag{33}$$

In this case, by using Equations (28)—(31), the theoretical total transmission coefficient is derived as $T_t = 0.7$.

As shown in Fig. 10, the ratio of the amplitude of the simulated transmitted wave to that of the incident wave is $12.2/17.65\approx0.69$. Both the arrival time of the wave and the amplitude attenuation ratio of the transmitted wave are in complete agreement with the theoretical solutions.

5. Simulations and comparative analyses

5.1. Samples with a crack outside the tunnel

In this experiment, a green sandstone from Zigong region of Sichuan Province of China was adopted. In research on fracture mechanics,

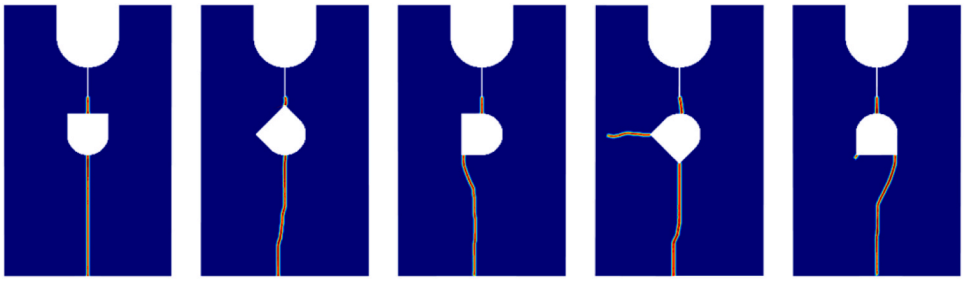

Fig. 14. The damage patterns predicted by XPD.

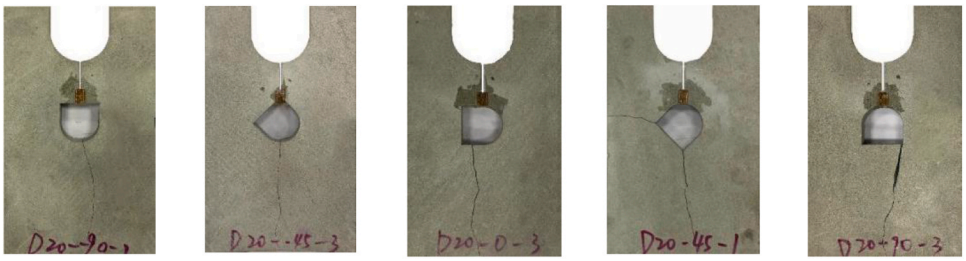

Fig. 15. The crack patterns from tests.

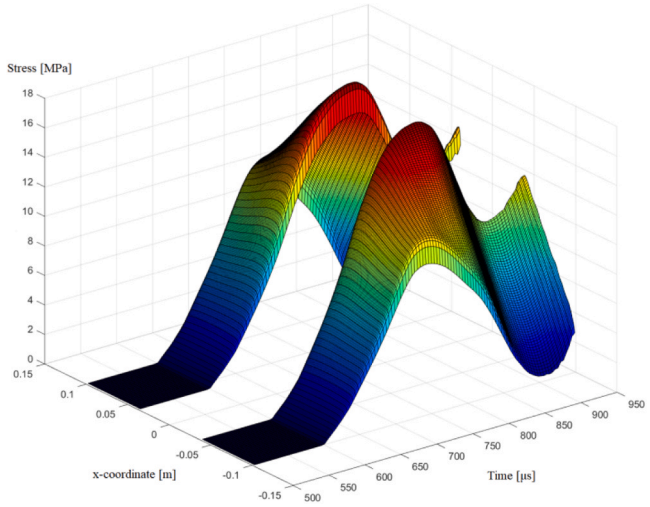

Fig. 16. The contact stress on the upper surface of the sample.

researchers have designed various configurations to study the dynamic fracture characteristics of rock materials, e.g. the crack through Brazilian disc [28], the notched semi-circle bend [29]. In traditional impact tests, the use of small-sized model may lead to unreality of stress waves due to the reflected wave from the sample's boundaries, leading to a large deviation from actual engineering scenarios. In underground spaces, the outer boundary of a tunnel can be approximated as infinite, with minimal wave reflection effects. Therefore, a larger model size is needed to reduce the impact of wave reflection [30–32]. Here, we conduct an experiment using a large single cleavage semicircle compression (LSCSC) specimen (200 mm × 325 mm × 30 mm) to study the dynamic behavior under impact loading. To achieve the ideal pre-crack, 1 mm thick hacksaw blade was used to obtain the pre-crack of all specimen.

5.1.1. *Evaluation of the model's predictive ability*

To validate the effectiveness of the model, we first simulated the crack growth in a sample without holes and compared the simulation results with experimental results. The schematic diagram of the model is exhibited in Fig. 11. The material parameters used in the numerical simulation are given in Table 2.

Clearly, the sample will start to crack at the tip of the prefabricated crack and extend downward vertically. Since the dynamic properties of materials are directly related to the propagation speed, this section mainly records and compares the crack propagation speeds. Fig. 12 shows the crack propagation speed simulated by the numerical system and the results recorded in the experiment, with the trends and numerical values being largely consistent.

5.1.2. *Simulation of the crack propagation*

To investigate the influence of impact loads from different directions on cracks near tunnels, this section adopts a simplified tunnel model to simulate the fracture behavior of rock materials. As shown in Fig. 13, the prefabricated crack length is 35 mm, with a U-shaped tunnel-like hole set 20 mm from the crack tip, and the center of the tunnel is 40 mm from the crack tip. The tunnel is initially placed horizontally and rotated counterclockwise around the center to form tunnel models at different angles. The stress waveform input at the upper end of the incident plate is the same as the incident wave in Fig. 2.

We used the proposed system to simulate tests for various tunnel angles, and the simulated damage patterns are shown in Fig. 14. The cracks generally show a trend of running through from top to bottom, with some angles (such as $\theta = 45^{\circ}$) showing laterally developing cracks, which are in good agreement with the experimental results in Fig. 15. With the help of this simulation model, we can not only reproduce the experimental results but, more importantly, also study the stress conditions of the structure under dynamic impact more specifically, analyzing the stresses at different times and structural positions, thereby providing effective protection or design references for structures that may be affected by dynamic impact waves in engineering practice.

In traditional dynamic impact simulations, stress waves are uniformly applied to the upper surface of the specimen, without considering the effects of material differences between the incident plate and the specimen, as well as the structural inhomogeneity of the specimen on stress loading. Fig. 16 illustrates a three-dimensional surface plot of the

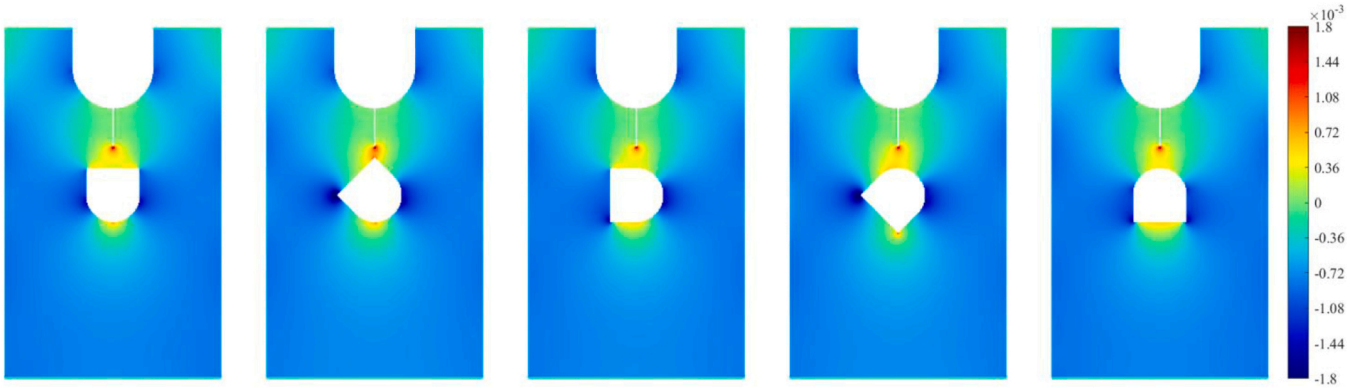

Fig. 17. The distribution of θ when the crack initiated for the first time.

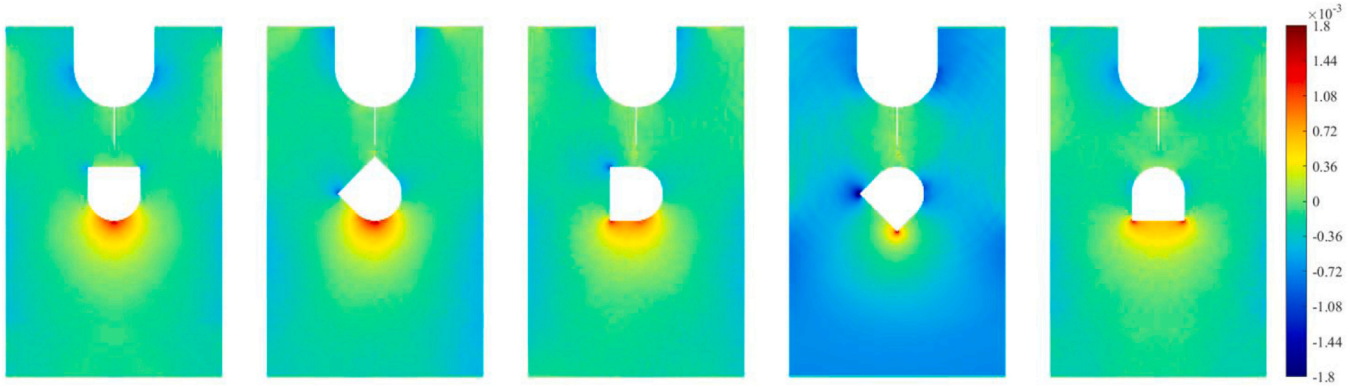

Fig. 18. The distribution of θ when the crack initiated for the second time.

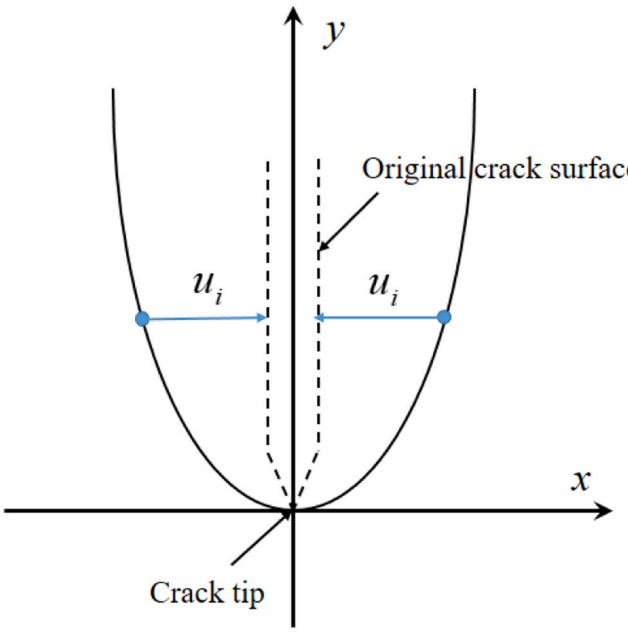

Fig. 19. Crack opening displacement.

force over time at the interface between the incident plate and the specimen. When the plate begin to contact the specimen, the stress increases uniformly. However, as time progresses, the stress on the inner part of the specimen becomes significantly greater than that on the outer edges. This model effectively demonstrates the non-uniformity of stress transmission at the contact surface, providing a more realistic reflection of the dynamic response process than simply applying dynamic forces on the upper surface of the specimen.

Since this experiment mainly explores the failure characteristics of materials, we utilize the convenience of the XPD model for calculating local strain to obtain the volumetric strain θ at the moment of crack initiation, which reflects the intensity of material volume change and is closely related to the tensile failure of materials. Fig. 17 provides a distribution map of θ at the moment of the first crack initiation. Since the stress wave equivalently applies a longitudinal compression wave to the structure, it also drives the lateral tension of the material. It can be seen that at the moment of the first crack initiation, the left and right sides of the tunnel are in a state of volume compression, while at the tip of the prefabricated crack, the volume expansion is most intense, and the part of the tunnel near the crack tip also shows significant volume expansion. It can be observed that, compared to the smooth surface of the tunnel, the corners and arches are more prone to significant volume compression or expansion.

We also recorded the strain distribution images at the moment of secondary crack initiation below the tunnel, as shown in Fig. 18. Since the crack above the tunnel has already run through, the concentrated stress above has been released, and the driving force for structural lateral tension is concentrated below the tunnel. In our tests, the secondary crack initiation occurs earliest at a tunnel angle of 45° , because at this angle, the corner of the tunnel faces downward, where the tensile resistance is the weakest, while at other angles, the downward-facing surfaces are relatively smooth and less prone to stress concentration. This also leads to the conclusion that when the tip of an underground structure aligns with the direction of stress wave propagation, the structure is more susceptible to failure.

5.1.3. *Calculation of dynamic stress intensity factor*

In the study of rock fractures, dynamic fracture toughness is a key parameter characterizing the ability of rocks to resist the initiation and propagation of dynamic cracks. It not only serves as an intrinsic mechanical parameter of rock dynamic fracture behavior, but also is an important indicator for evaluating the strength of rock masses. Therefore, dynamic fracture toughness plays an important role in revealing the dynamic failure mechanisms of rocks.

Based on fracture mechanics [33], the stress intensity factors (SIFs) are directly related to the crack opening displacement (as show in Fig. 19):

$$u(r_i, n) = \frac{8K_I(n,t)(1-\nu^2)}{E}\sqrt{\frac{r_i}{2\pi}} \tag{34}$$

where $K_I(n,t)$ is the mode I SIF at n^{th} point, and r_i is the distance from the point on the crack surface to the crack tip.

Eq. (34) can be rewritten as

$$K_I(n,t) = \frac{Eu(r_i,n)}{8(1-\nu^2)}\sqrt{\frac{2\pi}{r_i}} \tag{35}$$

The crack opening displacement can be obtained from numerical results. In this way, multiple groups of $K_I(n,t)$can be obtained. Finally, the least square method is adopted to fit and obtain the type I stress intensity factor $K_I(t)$ at the crack tip:

$$K_I(t) = \frac{\sum r_i \sum r_i K_I(n,t) - \sum r_i^2 \sum K_I(n,t)}{\left(\sum r_i\right)^2 - N\sum r_i^2} \tag{36}$$

where N is the number of points set on the crack surface. The larger the N is, the more accurate the SIF at the crack tip will be.

The dynamic stress intensity factors (DSIFs) exhibit distinct characteristics compared to their static counterparts during rapid crack propagation. Freund [34] established a fundamental relationship through theoretical analysis, demonstrating that for opening-mode crack growth under general loading conditions, the DSIFs can be expressed as the

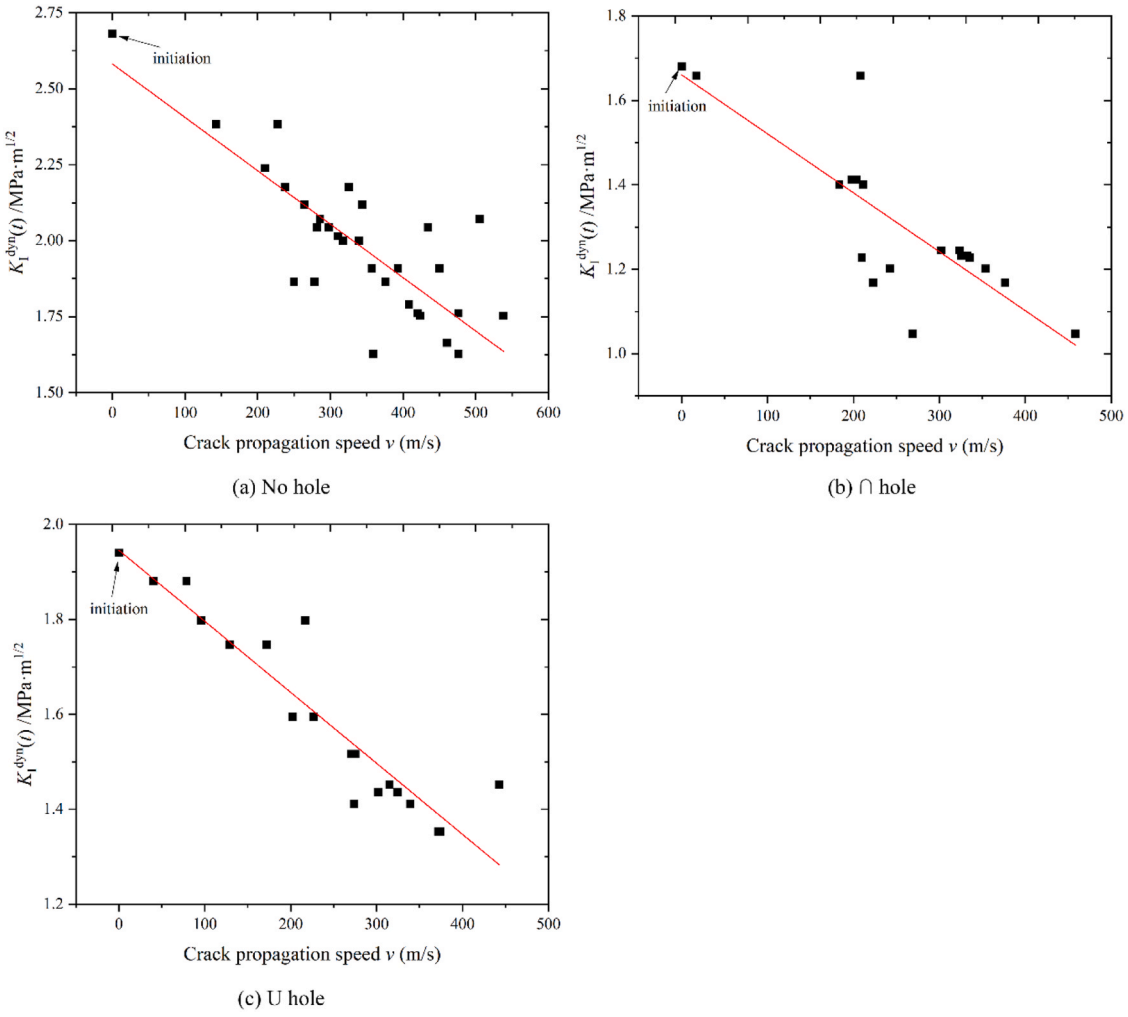

Fig. 20. Crack propagation speed versus fracture toughness.

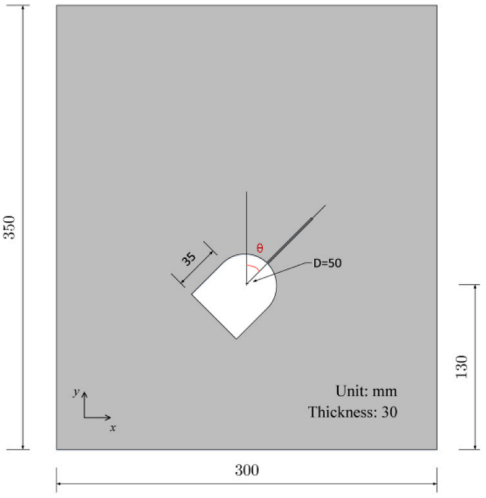

Fig. 21. The sample with a cracked tunnel.

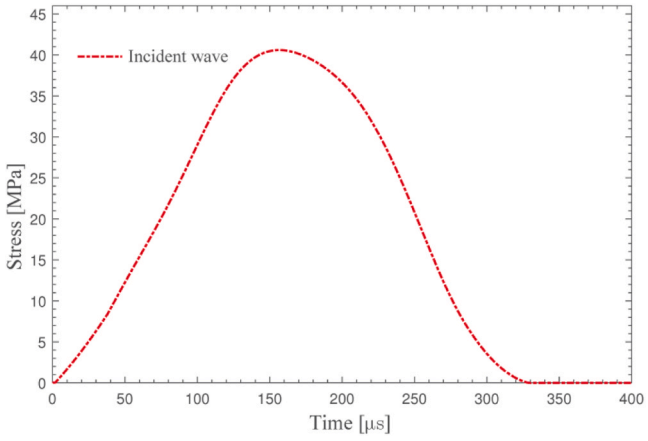

Fig. 22. The incident wave.

Table 3
Parameters used in the numerical simulations.

$E_{(GPa)}$	ν	$\rho_{(kg/m)}^{3}$	ℓ_c	$\delta_{(mm)}$	Δx (mm)
13.57	0.17	2265	0.0015	6	2

product of a universal velocity-dependent function $k(\mathrm{v})$ and the static stress intensity factor (SIF) corresponding to a stationary crack tip configuration:

$$K_I^{\mathrm{dyn}} = k(\mathrm{v})\cdot K_I$$
$$k(\mathrm{v}) \approx \left(1-\mathrm{v}/\mathrm{C}_R\right) \Big/ \sqrt{1-\mathrm{v}/\mathrm{C}_P} \tag{37}$$

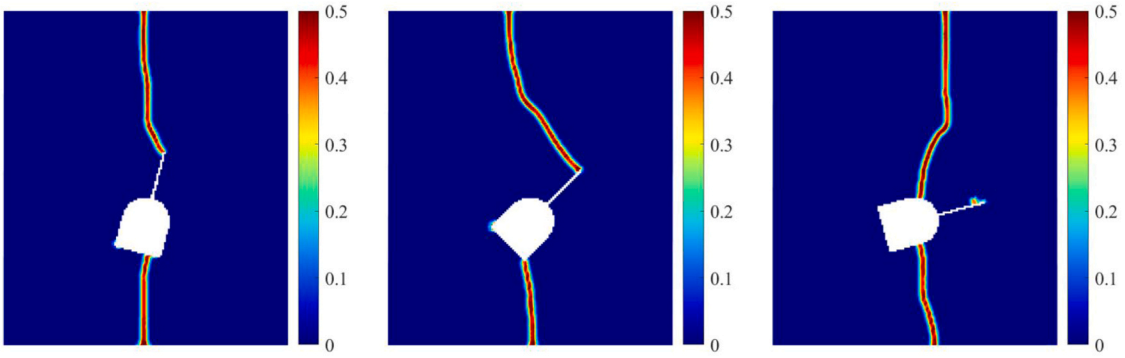

Fig. 23. The damage patterns predicted by XPD.

Fig. 24. The crack patterns from tests.

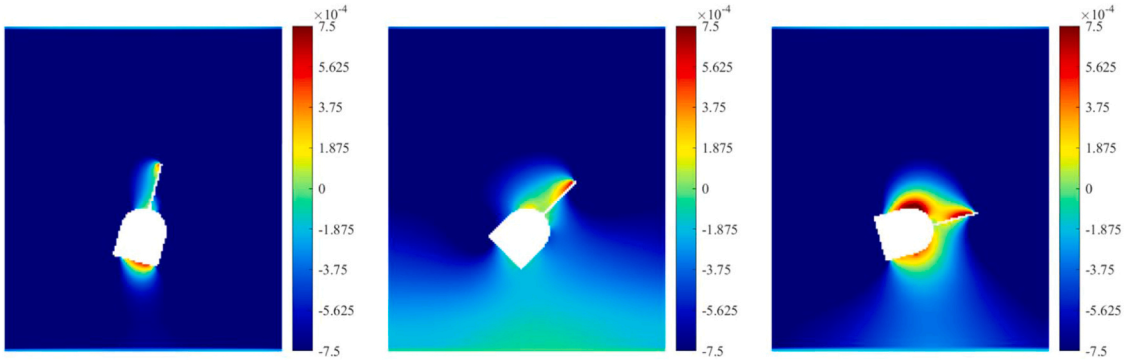

Fig. 25. The distribution of θ when the crack initiated.

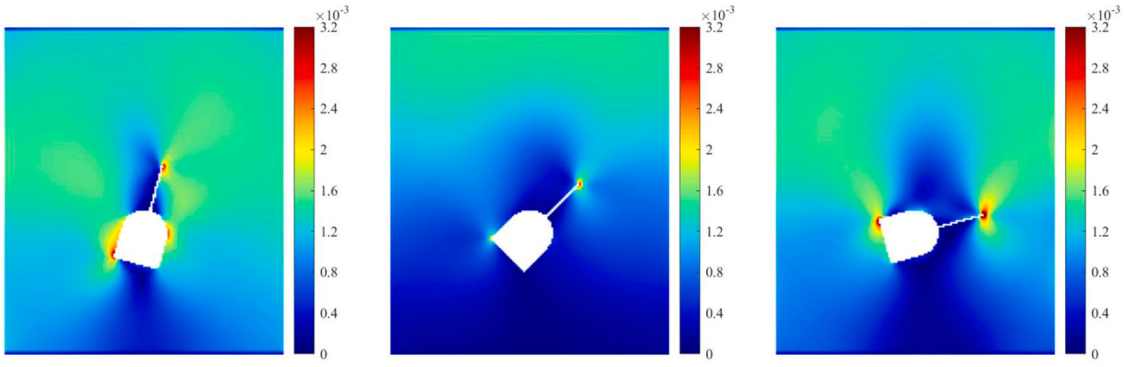

Fig. 26. The distribution of ε_{eq} when the crack initiated.

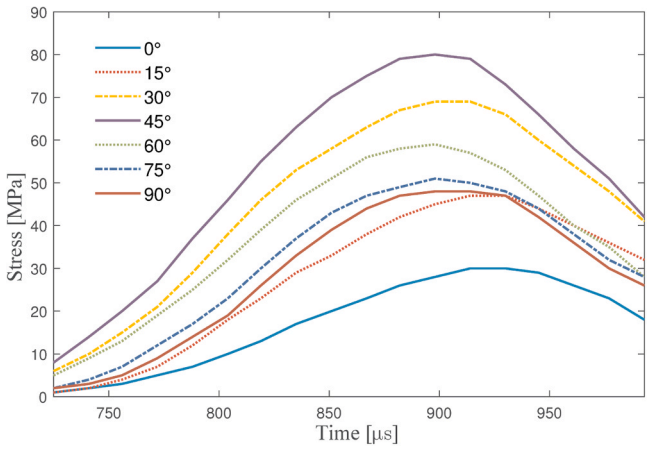

Fig. 27. The extreme values of σ_1 for different tunnel angles.

where K_I is the SIF of the corresponding static crack, K_I^{dyn} is the DSIF, and v is the crack propagation speed at the corresponding crack length. C_P and C_R are the P-wave and Rayleigh wave velocities of the green sandstone respectively, which were measured by using ultrasonic detector RSM-SY5(T).

In this study, we derive the displacement of the grid point at the moment of bond fracture in peridynamics and compute the fracture toughness of the crack using Eq. (36). By correlating these with physical experiments, the correction coefficient $k(\mathrm{v})$ is obtained. Subsequently, the dynamic stress intensity factor (DSIF) of rock materials is calculated using Equation Eq. (37), and the results are illustrated in Fig. 20. Our analysis reveals that the dynamic fracture toughness of rock materials is inversely proportional to the crack propagation velocity, with fitting curves exhibiting R^2 values all above 0.8262. Additionally, the crack initiation toughness is found to be greater than the crack propagation toughness.

Under identical impact conditions, different models exhibit varying dynamic fracture toughness, with the average fracture toughness following the order: no hole > U-hole specimen ($\theta = -90^\circ$) > ∩-hole specimen ($\theta = 90^\circ$). Specifically, for the no-hole specimen, the crack initiation toughness is 2.68 MPa·m$^{1/2}$, whereas for the U hole and ∩ -hole specimens, the crack initiation toughnesses are 1.94 MPa·m$^{1/2}$ and 1.67 MPa·m$^{1/2}$, respectively, representing decreases of 27.61 % and 37.69 % compared to no holed specimen. The presence of holes in the structure is observed to compromise both the structural safety and the crack initiation toughness.

It is noteworthy that the initiation toughness differs between the U hole and ∩ hole specimens, a discrepancy potentially attributable to the varying reflections of stress waves at the hole boundaries. In terms of propagation toughness, the U-hole test demonstrates greater toughness than the∩hole test. The superposition of reflected waves on incident waves makes crack initiation more difficult, thereby enhancing the fracture toughness. Regarding propagation toughness, the slower the crack growth velocity, the more difficult it is for crack growth. These findings are consistent with the principles in literature [35–38].

5.2. Samples with a crack connected to the tunnel

In engineering practice, cracks may not only appear in the nearby area of underground structures, but some may even penetrate and connect with the underground structures. Different from the previous section which mainly studied the influence of cracks outside the tunnel on the dynamic response of the tunnel, this section uses the proposed model to study the influence of the impact direction on the stability of the cracked tunnel, and observes the influence of the existence of connected cracks at different angles on the fracture mode and the stress of the tunnel. The experimental results for comparison are taken from [39]. In this sample, the cracked tunnel is set in the lower half, as shown in Fig. 21, and there is no U - shaped opening on the upper surface to induce opening fracture. The material parameters used in numerical simulations are shown in Table 3. By rotating the cracked tunnel in the sample to different directions, the influence of impacts from different directions on the cracked tunnel is reflected.

The form of incident wave is shown in Fig. 22. Similar to the previous section, we respectively present the fracture simulation diagrams in Fig. 23 and the experimental result diagrams in Fig. 24 under the conditions of $\theta = 15^\circ$, 45°and 75°. It can be seen from the figures that the results of the numerical simulation are consistent with the experimental results.

When rotating the tunnel, due to the inclination of the crack, we need to analyze the dominant factor for the crack growth, whether it is caused by tension or shear. Fig. 25 and Fig. 26 record the volumetric strain θ and the equivalent strain ε_{eq} at the moment of crack initiation, which are related to tensile and shear-dominated failure mechanisms, respectively. It can be seen that the area with a larger θ coincides with the location of crack initiation ，while no obvious crack development occurs in the area with a larger ε_{eq}.

To assess the impact of different impact directions on the cracked tunnel, we monitor the curve of the maximum principal stress σ_1 around the tunnel over time. A consistent stress wave is introduced from the incident plate, under the assumption that no additional damage occurs during wave propagation. The tunnel is rotated from 0° to 90° ，and the extreme value of σ_1 at each point around the tunnel is recorded at each moment. The resulting curve is presented in Fig. 27. It is evident that the curve peaks when $\theta = 45^\circ$ ，signifying the highest risk when the stress wave propagates along the inclined 45° direction of this fractured tunnel. Conversely, the curve reaches its lowest point when the stress wave propagates parallel to the crack ($\theta = 0^\circ$), indicating a relatively safer condition for the tunnel.

6. Conclusions

This study systematically investigated the dynamic fracture behavior of holed rock specimens under impact loading through a combined experimental and numerical approach. The key findings are summarized as follows.

1. The drop-weight impact system, incorporating incident and transmission plates, was successfully modeled to replicate realistic stress wave propagation. A comprehensive incident-sample-transmission model was essential to capture the non-uniform stress loading on sample boundaries.
2. The XPD model demonstrated robust capability in simulating dynamic crack propagation and failure modes in elastic-brittle materials. The model enables accurate predictions of crack initiation, branching, and velocity. Its simplicity in parameterization and its alignment with physical tests highlight its potential for engineering applications.
3. Tunnel-like holes significantly reduced the fracture toughness and altered the crack paths. Specimens with tunnels oriented at 45° relative to the stress wave direction exhibited the highest susceptibility to failure due to intensified tensile stress concentrations at tunnel corners. These findings emphasize the importance of geometric optimization in tunnel design to mitigate stress wave-induced hazards.

This study offers insights for underground engineering, particularly in predicting failure zones and optimizing tunnel orientations under dynamic loads. This research bridges experimental and computational approaches, advancing the understanding of dynamic fracture mechanics in holed rock structures. It also provides a promising tool for

assessing structural stability, guiding hazard prevention strategies, and informing design standards for rock masses with natural or artificial defects.

CRediT authorship contribution statement

Peng Ying: Writing – original draft, Visualization, Validation, Methodology, Investigation, Formal analysis, Data curation, Conceptualization. **Yu Zhao:** Writing – review & editing, Investigation, Formal analysis. **Junchen Zhang:** Validation, Formal analysis, Data curation. **Weijian Li:** Writing – review & editing, Visualization, Validation, Software, Methodology, Investigation, Funding acquisition, Data curation. **Yiqiang Zhao:** Resources, Project administration. **Zheming Zhu:** Writing – review & editing, Funding acquisition. **Yanliang Du:** Resources, Project administration, Funding acquisition.

Declaration of Competing Interest

The authors declare that they have no known competing financial interests or personal relationships that could have appeared to influence the work reported in this paper.

Acknowledgements

This work was financially supported by the National Natural Science Foundation of China (Grant Nos. 12402483, 52078467, 52204104, 12272247), China Postdoctoral Science Foundation (Grant No. 2024M752113), Major R&D project of Zhejiang Provincial Department of Transportation under (Grant no. 2025ZD001).

References

[1] M. Mousavi Nezhad, Q.J. Fisher, E. Gironacci, M. Rezania, Experimental study and numerical modeling of fracture propagation in shale rocks during Brazilian disk test, Rock. Mech. Rock. Eng. 51 (2018) 1755–1775.
[2] J. Shang, L.J. West, S.R. Hencher, Z. Zhao, Geological discontinuity persistence: implications and quantification, Eng. Geol. 241 (2018) 41–54.
[3] R. Cao, R. Yao, J. Meng, Q. Lin, H. Lin, S. Li, Failure mechanism of non-persistent jointed rock-like specimens under uniaxial loading: laboratory testing, Int. J. Rock. Mech. Min. Sci. 132 (2020) 104341.
[4] Q. Lin, P. Cao, J. Meng, R. Cao, Z. Zhao, Strength and failure characteristics of jointed rock mass with double circular holes under uniaxial compression: insights from discrete element method modelling, Theor. Appl. Fract. Mech. 109 (2020) 102692.
[5] Y.X. Yang kezhi, Shock waves propagation inside tunnels, Explos. Shock Waves 23 (2003) 37–40.
[6] J. Xu, Z. Li, Damage evolution and crack propagation in rocks with dual elliptic flaws in compression, Acta Mech. Solid. Sin. 30 (2017) 573–582.
[7] Q. Zhang, X.-P. Zhang, S.-Q. Yang, A numerical study of acoustic emission characteristics of sandstone specimen containing a hole-like flaw under uniaxial compression, Eng. Fract. Mech. 242 (2021) 107430.
[8] P.L.P. Wasantha, D. Bing, S.Q. Yang, T. Xu, Numerical modelling of the crack-pore interaction and damage evolution behaviour of rocklike materials with pre-existing cracks and pores, Int. J. Damage Mech. 30 (2020) 720–738.
[9] P. Jia, C.A. Tang, Numerical study on failure mechanism of tunnel in jointed rock mass, Tunn. Undergr. Space Technol. 23 (2008) 500–507.
[10] M. Wang, G. Ma, F. Wang, Numerically investigation on blast-induced wave propagation in catastrophic large-scale bedding rockslide, Landslides 18 (2020) 785–797.
[11] W.C. Zhu, Z.H. Li, L. Zhu, C.A. Tang, Numerical simulation on rockburst of underground opening triggered by dynamic disturbance, Tunn. Undergr. Space Technol. 25 (2010) 587–599.
[12] L. Zhou, Z. Zhu, M. Wang, P. Ying, Y. Dong, Dynamic propagation behavior of cracks emanating from tunnel edges under impact loads, Soil Dyn. Earthq. Eng. 105 (2018) 119–126.
[13] X. Li, C. Li, W. Cao, M. Tao, Dynamic stress concentration and energy evolution of deep-buried tunnels under blasting loads, Int. J. Rock. Mech. Min. Sci. 104 (2018) 131–146.
[14] P. Ying, Z. Zhu, L. Ren, S. Deng, C. Niu, D. Wan, et al., Deterioration of dynamic fracture characteristics, tensile strength and elastic modulus of tight sandstone under dry-wet cycles, Theor. Appl. Fract. Mech. 109 (2020) 102698.
[15] P. Ying, Z. Zhu, L. Zhou, M. Wang, Y. Dong, H. Qiu, The effect of loading rates on crack dynamic behavior under medium–low speed impacts, Acta Mech. Solid. Sin. 32 (2018) 93–104.
[16] S.A. Silling, Reformulation of elasticity theory for discontinuities and long-range forces, J. Mech. Phys. Solids 48 (2000) 175–209.
[17] S.A. Silling, E. Askari, A meshfree method based on the peridynamic model of solid mechanics, Comput. Struct. 83 (2005) 1526–1535.
[18] T. Ni, M. Zaccariotto, Q.-Z. Zhu, U. Galvanetto, Static solution of crack propagation problems in Peridynamics, Comput. Methods Appl. Mech. Eng. 346 (2019) 126–151.
[19] H. Yu, X. Chen, Y. Sun, A generalized bond-based peridynamic model for quasi-brittle materials enriched with bond tension–rotation–shear coupling effects, Comput. Methods Appl. Mech. Eng. 372 (2020) 113405.
[20] Y. Tong, W.-Q. Shen, J.-F. Shao, An adaptive coupling method of state-based peridynamics theory and finite element method for modeling progressive failure process in cohesive materials, Comput. Methods Appl. Mech. Eng. 370 (2020) 113248.
[21] Y. Wang, X. Zhou, Y. Shou, The modeling of crack propagation and coalescence in rocks under uniaxial compression using the novel conjugated bond-based peridynamics, Int. J. Mech. Sci. 128-129 (2017) 614–643.
[22] Q.-Z. Zhu, T. Ni, Peridynamic formulations enriched with bond rotation effects, Int. J. Eng. Sci. 121 (2017) 118–129.
[23] W.-J. Li, Q.-Z. Zhu, T. Ni, A local strain-based implementation strategy for the extended peridynamic model with bond rotation, Comput. Methods Appl. Mech. Eng. 358 (2020) 112625.
[24] W.-J. Li, T. You, T. Ni, Q.-Z. Zhu, L.H. Poh, The extended peridynamic model for elasto-plastic and/or fracture problems, Int. J. Numer. Methods Eng. 123 (21) (2022) 5201–5229.
[25] W.-J. Li, Q.-Z. Zhu, Y.-L. Du, J.-F. Shao, An extended bond-based peridynamic model with bond transverse deformation effects for quasi-brittle rocks, Int. J. Rock. Mech. Min. Sci. 190 (2025) 106099.
[26] E. Rougier, A. Munjiza, N.W.M. John, Numerical comparison of some explicit time integration schemes used in DEM, FEM/DEM and molecular dynamics, Int. J. Numer. Methods Eng. 61 (6) (2004) 856–879.
[27] N.M. Newmark, A method of computation for structural dynamics, J. Eng. Mech. Div. 85 (3) (1959) 67–94.
[28] Q.Z. Wang, F. Feng, M. Ni, X.P. Gou, Measurement of mode I and mode II rock dynamic fracture toughness with cracked straight through flattened Brazilian disc impacted by split Hopkinson pressure bar, Eng. Fract. Mech. 78 (2011) 2455–2469.
[29] W. Yao, K. Xia, Dynamic notched semi-circle bend (NSCB) method for measuring fracture properties of rocks: fundamentals and applications, J. Rock. Mech. Geotech. Eng. 11 (2019) 1066–1093.
[30] P. Ying, Z. Zhu, F. Wang, M. Wang, C. Niu, L. Zhou, The characteristics of dynamic fracture toughness and energy release rate of rock under impact, Measurement 147 (2019) 106884.
[31] L. Zhou, Z. Zhu, H. Qiu, X. Zhang, L. Lang, Study of the effect of loading rates on crack propagation velocity and rock fracture toughness using cracked tunnel specimens, Int. J. Rock. Mech. Min. Sci. 112 (2018) 25–34.
[32] M. Wang, Z. Zhu, Y. Dong, L. Zhou, Study of mixed-mode I/II fractures using single cleavage semicircle compression specimens under impacting loads, Eng. Fract. Mech. 177 (2017) 33–44.
[33] A.T. Zehnder, Fracture Mechanics, Springer Science & Business Media, 2012.
[34] L.B. Freund, Crack propagation in an elastic solid subjected to general loading — I. Constant rate of extension, J. Mech. Phys. Solids 20 (1972) 129–140.
[35] D. Wan, Z. Zhu, R. Liu, B. Liu, J. Li, Measuring method of dynamic fracture toughness of mode I crack under blasting using a rectangle specimen with a crack and edge notches, Int. J. Rock. Mech. Min. Sci. 123 (2019) 104104.
[36] R. Liu, Z. Zhu, M. Li, B. Liu, D. Wan, Study on dynamic fracture behavior of mode I crack under blasting loads, Soil Dyn. Earthq. Eng. 117 (2019) 47–57.
[37] P. Ying, Z. Zhu, L. Zhou, Y. Fan, Y. Dong, M. Wang, Testing method of rock dynamic fracture toughness using large single cleavage semicircle compression specimens, J. Test. Eval. 48 (5) (2020) 20170702.
[38] X. Wang, Z. Zhu, M. Wang, P. Ying, L. Zhou, Y. Dong, Study of rock dynamic fracture toughness by using VB-SCSC specimens under medium-low speed impacts, Eng. Fract. Mech. 181 (2017) 52–64.
[39] L. Zhou, Z. Zhu, Y. Dong, et al., The influence of impacting orientations on the failure modes of cracked tunnel, Int. J. Impact Eng. 125 (2019) 134–142.

Peng Ying received his PhD degree from College of Architecture and Environment, Sichuan University, Chengdu, China. He is a member of the Chinese Society of Mechanics. His research interests are in the mechanical behaviour of deep rock, rock fracture mechanics, blasting, and tunnelling. He focuses on the application of advanced experimental and numerical methods in investigating the dynamic response of deep rock. He has published more than 30 technical papers in Rock mechanics and Rock engineering, Tunnelling and Underground Space Technology, Engineering Fracture Mechanics, International Journal of Rock Mechanics and Mining Science et al.